




# Ultrathin composite electrolyte with multifunctional skeleton for solid-state lithium metal batteries

Dongmei Zhang, Dingrong Long, Jiangping Zhang, Jiaxin Tu, Baoyi wang, Rubing Xu, Kunda Yang, Qianxiao Fan, Wendi Zhang, Lehao Liu<sup>\*</sup>, Meicheng Li<sup>\*\*</sup> 

State Key Laboratory of Alternate Electrical Power System with Renewable Energy Sources, School of New Energy, North China Electric Power University, Beijing, 102206, China

## HIGHLIGHTS

- A 10- $\mu\text{m}$ -thick composite electrolyte is developed via solution infusion method.
- Composite electrolyte shows high room-temperature  $\text{Li}^+$  transference number of 0.83.
- LiF-rich SEI layer inhibits interfacial side reactions and dendrite growth.

## ARTICLE INFO

### Keywords:

Multifunctional supporting skeleton  
Lithium metal batteries  
Ion transference number  
Composite electrolyte

## ABSTRACT

Succinonitrile (SN)-based electrolytes have emerged as promising candidates for lithium metal batteries (LMBs) due to their high ionic conductivity and thermal stability. However, the limited mechanical robustness, low reduction resistance, and residual free SN molecules can damage the electrochemical performance of batteries. Herein, an ultrathin (10  $\mu\text{m}$ ) yet mechanically robust composite electrolyte is developed by introducing a rigid multifunctional supporting skeleton, fabricated through in situ growth of zeolitic imidazolate framework (ZIF) nanoparticles within a three-dimensional (3D) aramid nanofibers (ANF) network. The rigid supporting skeleton functionalized with ZIF-67 nanoparticles can selectively absorb lithium salt anions to regulate  $\text{Li}^+$  transport. The well-designed composite electrolyte exhibits a high  $\text{Li}^+$  ionic conductivity of  $3 \times 10^{-4} \text{ S cm}^{-1}$  and a  $\text{Li}^+$  transference number of 0.83 at room temperature. Meanwhile, the rigid multifunctional skeleton effectively mitigates side reactions between SN and lithium metal through inducing the formation of the LiF-rich solid electrolyte interphase layer. As a result, the composite electrolyte-based  $\text{Li}||\text{Li}$ ,  $\text{Li}||\text{LiFePO}_4$  and  $\text{Li}||\text{LiNi}_{0.6}\text{Co}_{0.2}\text{Mn}_{0.2}\text{O}_2$  cells show superior electrochemical performance at room temperature. Notably, the  $\text{Li}||\text{LiFePO}_4$  cells also deliver stable performance at low temperature. This design offers an efficient, scalable fabrication method for ultrathin solid-state electrolyte-based highly stable and safe LMBs.

## 1. Introduction

Lithium-ion batteries (LIBs) have found widespread applications in electric vehicles and portable electronic devices [1–3]. However, the energy density of present LIBs needs to be substantially enhanced to meet future sustainable energy requirements. Lithium metal batteries (LMBs) are regarded as one of the most promising candidates for next-generation energy storage systems, owing to the ultra-low reduction potential and exceptionally high theoretical specific capacity of

lithium metal anodes [4,5]. Nevertheless, the practical application of LMBs is still hindered by critical challenges, including safety risks and limited cycle life, primarily attributed to the use of flammable liquid electrolytes and uncontrolled lithium dendrite growth. Replacing liquid electrolytes with solid-state electrolytes (SSEs) could mitigate the risks of leakage and combustion of liquid electrolytes. SSEs are commonly divided into inorganic electrolytes and polymer electrolytes. Inorganic electrolytes generally exhibit high ionic conductivity at ambient temperature and excellent chemical stability against lithium metal [6].

\* Corresponding author.

\*\* Corresponding author.

E-mail addresses: [lehaoliu@ncepu.edu.cn](mailto:lehaoliu@ncepu.edu.cn) (L. Liu), [mcli@ncepu.edu.cn](mailto:mcli@ncepu.edu.cn) (M. Li).

<https://doi.org/10.1016/j.jpowsour.2025.238312>

Received 16 July 2025; Received in revised form 21 August 2025; Accepted 2 September 2025

Available online 17 September 2025

0378-7753/© 2025 Elsevier B.V. All rights are reserved, including those for text and data mining, AI training, and similar technologies.

However, their practical application is significantly hindered by high interfacial resistance at the electrode/electrolyte interfaces due to poor solid/solid contact. Polymer electrolytes have flexibility, good processibility and low electrode/electrolyte interface resistance [7–9]. But the low room-temperature ionic conductivity and poor lithium dendrites suppression capability of polymer electrolytes have severely hindered their practical application [10–12]. Therefore, developing an electrolyte with high ionic conductivity and good lithium metal compatibility is crucial for practical application of solid-state lithium metal batteries.

Succinonitrile (SN)-based plastic crystal electrolytes, a mixture of plastic crystals and lithium salts, have recently gained increasing attentions with high ionic conductivity and thermal stability. Moreover, SN remains solid-state stability across a wide temperature range from the transition temperature ( $-40\text{ }^{\circ}\text{C}$ ) to the melting temperature ( $60\text{ }^{\circ}\text{C}$ ), ensuring inherent safety at ambient conditions while preventing leakage of liquid electrolyte. However, when implemented in LMBs, SN-based electrolytes encounter two fundamental challenges: (1) SN is incompatible with lithium metal, especially lithium-induced polymerization of  $\text{C}\equiv\text{N}$  groups generate insulating interfacial layers, which leads to poor electrode-electrolyte contact and severe capacity degradation in LMBs. (2) SN suffers from insufficient mechanical strength, which further deteriorates upon lithium salt dissolution, making it unsuitable as a self-supporting solid electrolyte layer.

Recently, SN-based electrolytes integrated with a host matrix or support skeleton have emerged as promising solid-state electrolytes, offering a viable solution to the limitation of conventional SN-based electrolytes [13–17]. The introduction of suitable host polymers not only enhances the film-forming ability of SN-based electrolytes but also coordinates with SN to suppress its decomposition under the catalytic influence of lithium metal. However, the host polymer content significantly exceeded that of SN, which could disrupt the molecular distribution, crystallinity, and configuration of SN, thereby degrading the ionic conductivity of the electrolyte. The incorporation of support skeleton into SN-based electrolytes is also an effectively method to achieve excellent electrochemical performance of batteries. The inorganic skeleton (e.g.,  $\text{Li}_{6.75}\text{La}_3\text{Zr}_{1.75}\text{Ta}_{0.25}\text{O}_{12}$ ), as an active filler, not only establishes continuous  $\text{Li}^+$  conduction pathways but also enhances the overall electrochemical stability of batteries. However, the intrinsic brittleness of the inorganic skeletons limits the processability of composite electrolytes, typically resulting that the thickness of the composite electrolytes is commonly higher than  $100\text{ }\mu\text{m}$ . The thickness is closely related to the electrochemical performance of batteries. Thinner composite electrolytes can shorten the distance for  $\text{Li}^+$  diffusion in composite electrolytes to greatly lower ohmic resistance, improving the electrochemical performance of batteries. The porous organic skeletons (e.g., nonwoven fabrics, polyimide nanofibers and polyethylene separators) offer superior mechanical flexibility, enabling the fabrication of thin ( $<50\text{ }\mu\text{m}$ ) composite electrolytes with enhanced structural integrity [18–20]. Nonetheless, these organic skeletons also exhibit a notable limitation, as they show low ionic conductivity at room temperature and insufficient lithium dendrite suppression capability. Thus, designing an ultrathin ( $<10\text{ }\mu\text{m}$ ) SN-based composite electrolyte with high mechanical strength against lithium metal is a key challenge for practical LMBs applications.

Aramid nanofibers (ANFs) with high mechanical strength and low electro-conductivity have been used as multifunctional nanofillers to improve the electrical and mechanical properties of the solid polymer electrolytes. Moreover, the ANFs chains with lithiophilic polar functional groups (i.e., amide groups) can easily interact with  $\text{Li}^+$  and participate in the  $\text{Li}^+$  transport. On the other hand, zeolitic imidazolate framework (ZIF) exhibit ultrahigh porosity, large surface areas, accessible coordinative unsaturated sites, and excellent chemical and solvent stability. Benefiting from the mature technology for large-scale fabrication of ANFs and ZIF, these materials are widely used as additives for composite electrolytes. Notably, ZIF-67, a cobalt-based zeolitic imidazolate framework composed of  $\text{Co}^{2+}$  ions and 2-methylimidazolate

linkers, exhibits dual functionality: it simultaneously facilitates  $\text{Li}^+$  transport through anion confinement, while effectively suppresses lithium dendrite growth and minimizes undesirable side reactions between SN and lithium metal [21–23]. In this work, we adopt a strategy that integrates a rigid multifunctional skeleton to design an ultrathin composite electrolyte membrane with an ultrahigh  $\text{Li}^+$  transference number. The rigid multifunctional skeleton is constructed through in situ growth of ZIF-67 nanoparticles on ANF network. The SN-lithium bis (trifluoromethyl sulphonyl) imide (LiTFSI) electrolyte is filled into the rigid functional skeleton via facile and scalable solution infusion method. The three-dimensional (3D) ANF network establish continuous  $\text{Li}^+$  transport pathways, while the in situ grown ZIF-67 nanoparticles selectively complex with  $\text{TFSI}^-$  anions. This synergistic effect promotes  $\text{Li}^+$  dissociation and enhances ion mobility, ultimately creating a rigid, fast  $\text{Li}^+$  conduction network with uninterrupted pathways. The composite electrolyte membrane demonstrates excellent electrochemical properties, including high room-temperature ionic conductivity of  $3\times 10^{-4}\text{ S cm}^{-1}$ ,  $\text{Li}^+$  transference number of 0.83 and mechanical strength (a tensile stress of  $10.3\text{ MPa}$  with a tensile strain of  $7.8\%$ ). Moreover, the in situ grown ZIF-67 nanoparticles effectively suppress lithium dendrite formation and mitigate side reactions between SN and lithium metal through inducing the formation of the LiF-rich solid electrolyte interphase (SEI) layer. To evaluate the practical applicability of the ultrathin composite electrolyte, the  $\text{Li}|\text{LiNi}_{0.6}\text{Co}_{0.2}\text{Mn}_{0.2}\text{O}_2$  cells with an ultrahigh active mass loading of  $10\text{ mg cm}^{-2}$  exhibit excellent cycling stability and rate performance at room temperature. This work offers a facile and scalable strategy for fabricating ultrathin solid electrolyte with ultrahigh  $\text{Li}^+$  transference number, demonstrating significant potential for practical implementation in high-performance solid-state lithium metal batteries.

## 2. Experimental section

### 2.1. Materials

Aramid fibers (Kevlar 69) were purchased from DuPont Company. Dimethyl sulfoxide (DMSO), *tert*-Butyl alcohol (TBA), potassium hydroxide (KOH), succinonitrile (SN), anhydrous methanol ( $\text{CH}_3\text{OH}$ , 99.5%), cobalt nitrate hexahydrate ( $\text{Co}(\text{NO}_3)_2\cdot 6\text{H}_2\text{O}$ , 98.5%), ethanol (99%), *N*-methyl-2-pyrrolidone (NMP, 99.8%), carbon black (Super P, battery grade), lithium iron phosphate ( $\text{LiFePO}_4$ , battery grade) and bis (trifluoromethane)sulfonimide lithium salt (LiTFSI) were obtained from Aladdin Co., Ltd. 2-methylimidazole ( $\text{C}_4\text{H}_6\text{N}_2$ , 98%) was obtained from Mackli Co., Ltd. Fluoroethylene carbonate (FEC) and multi-walled carbon nanotubes were purchased from DoDoChem Co., Ltd.

### 2.2. Preparation of the skeleton films

4.00 g long Kevlar 69 microfiber, 4.00 g KOH and 200.00 mL DMSO were stirred for about 7 days at room temperature until the generation of a dark red ANF dispersion. The fabrication process of the ANF network films was via a facial blade coating method followed by a freeze-drying process. In the blade coating process, a high concentration of ANF/DMSO dispersion was deposited on the glass plate. Then, the ANF films were formed by immersing into deionized (DI) water for 12 h by protonation process. Subsequently, a modified freeze-drying method was applied to dry ANF films using a mixture DI water and *tert*-butyl alcohol (mass ratio of 1:1) as the solvent system, promoting the delicate structures of hydrogels from breaking or degenerating. The porous ANF films with 3D interconnect networks were obtained after drying 72 h.

2.0 g of  $\text{Co}(\text{NO}_3)_2\cdot 6\text{H}_2\text{O}$  was dissolved in 30 mL of  $\text{CH}_3\text{OH}$  to form solution A. 4.6 g  $\text{C}_4\text{H}_6\text{N}_2$  was dissolved in 30 mL of  $\text{CH}_3\text{OH}$  form solution B. ANF network films were immersed in solution A for 0.5 h, and then, the ANF network films were immersed in solution B for 0 h, 1 h, 2 h and 3 h. These films were then removed and washed several times with ethanol, followed by drying at  $45\text{ }^{\circ}\text{C}$  in a vacuum oven for 12 h (i.e.,

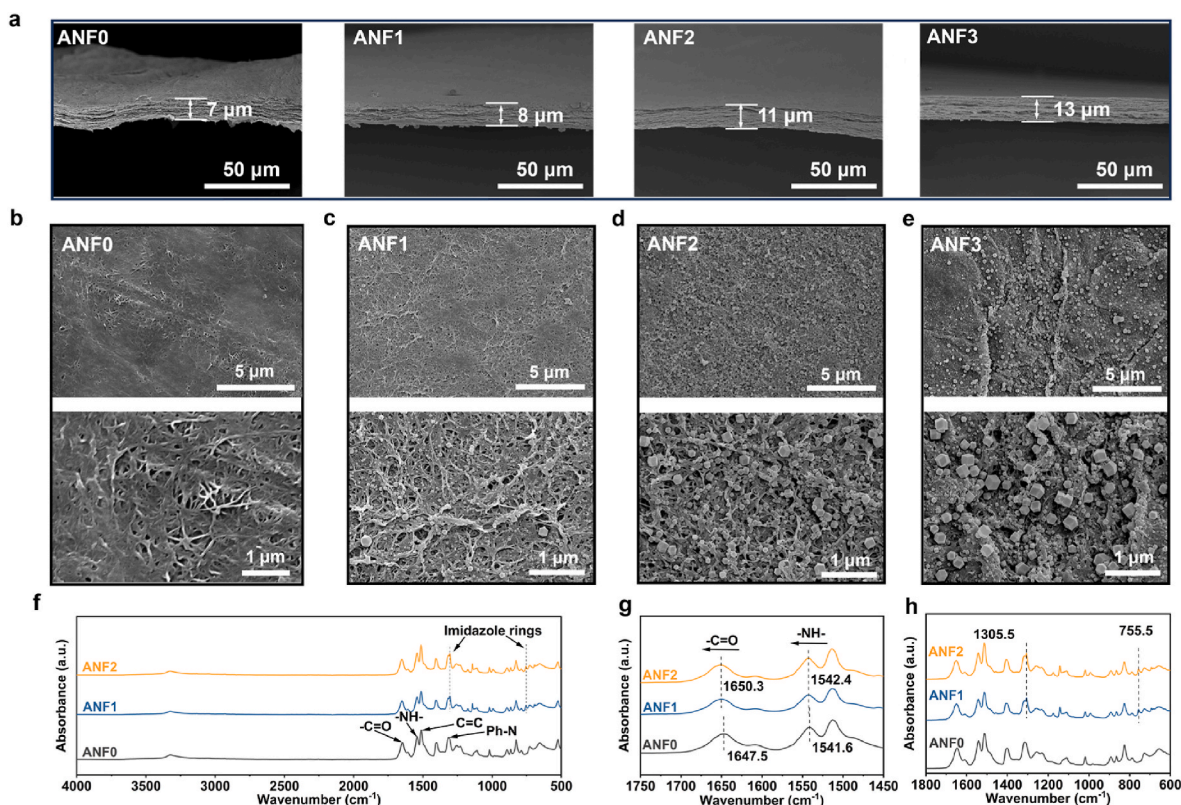


Fig. 1. (a) Cross-sectional SEM image of the ANF skeleton films. Surface SEM images of the ANF skeleton films: (b) ANF0, (c) ANF1, (d) ANF2 and (e) ANF3. (f), (g) and (h) FTIR spectra of ANF0, ANF1 and ANF2 films.

ANF0, ANF1, ANF2 and ANF3).

### 2.3. Preparation of the composite electrolyte membranes

The composite electrolyte membranes were obtained by a solution-immersing method. Molten SN-LiTFSI electrolyte was prepared by mixing SN and LiTFSI with a molar ratio of 20:1 and melting them into liquid through heating above 60 °C and stirring for 12 h. Then, the prepared ANF skeleton films were immersed into the SN-LiTFSI electrolyte for 12 h. After removing the excess SN-LiTFSI electrolyte by filter paper, the composite electrolytes were obtained (i.e., CPE0, CPE1 and CPE2). Subsequently, the above electrolyte membranes were placed under vacuum at 45 °C for a week to remove as much the residual SN-LiTFSI solution as possible. Finally, all the electrolyte films were further placed in argon-filled glove box for at least 48 h before different characterizations and measurements.

### 2.4. Material characterizations

A SU8010 field emission scanning electron microscope (SEM) combined with an energy dispersive spectroscopy (EDS) was used to observe the surface and cross-section morphology and the element composition of the composite electrolytes. A D8 Focus X-ray diffractometer (XRD) was used to explore the effect of the ANF framework on the crystallinity of the CPE. The mechanical tensile properties of the electrolyte membranes were measured by a GOTECH AI-7000-ST mechanical tester with an ascending velocity of 2 mm min<sup>-1</sup>. A Thermo Scientific Nicolet iS50 Fourier transform infrared (FT-IR) spectrometer was used to detect the functional groups and chemical bonds of the ANF framework, SN, LiTFSI and CPE. A NETZSCH DSC 200 F3 differential scanning calorimeter (DSC) was used to test the crystallinity of the CPE in the range of -90–110 °C. Thermo Scientific K-Alpha X-ray photoelectron spectroscopy (XPS) was performed on the lithium metal surfaces after the

electrochemical cycling.

### 2.5. Electrochemical measures

Symmetric or asymmetric cells were prepared by loading the electrolytes into CR2032 coin cells for electrochemical characterizations. A Zahner Zennium electrochemical workstation was utilized to test the impedance of the symmetrical stainless steel (SS)|CPE|SS batteries in the frequency from 10<sup>6</sup> to 10<sup>-2</sup> Hz at 30–80 °C. The ionic conductivity ( $\sigma$ ) was determined from the following formula:

$$\sigma = \frac{L}{S \cdot R}$$

where  $L$  is the thickness of the film,  $S$  is the conducting area, and  $R$  is the resistance. The linear sweep voltammetry (LSV) tests were applied by a CHI660E electrochemical workstation in the asymmetric Li|CPE|SS cells with a scan rate of 1 mV s<sup>-1</sup> at 30 °C. The Li ion transference number ( $t_{Li}^+$ ) was measured by time ampere method and AC impedance spectroscopy. A potential of 10 mV was applied for a polarization time of 2000 s. According to the formula:

$$\tau_{Li^+} = I_{ss}(\Delta V - I_0 R_0) / I_0(\Delta V - I_{ss} R_{ss})$$

where  $I_0$ ,  $\Delta V$  and  $I_{ss}$  were initial state current, 10 mV polarization potential and steady-state current, respectively.  $R_0$  and  $R_{ss}$  were the resistances at the start and completing time, respectively.

LAND CT2001A battery test system was used for electrochemical measurements. Symmetric Li|CPE|Li cells were assembled to test the critical current density and cyclic stability. LiFePO<sub>4</sub> (LFP) cathodes were composed of 80 wt% LFP, 10 wt% PVDF, 9.7 wt% carbon black and 0.3 wt% multi-walled carbon nanotubes. The active LFP content of the electrodes was about 4.0 mg cm<sup>-2</sup>. LiNi<sub>0.6</sub>Co<sub>0.2</sub>Mn<sub>0.2</sub>O<sub>2</sub> (NCM622) cathodes were purchased by commercial electrode tape with 10 mg



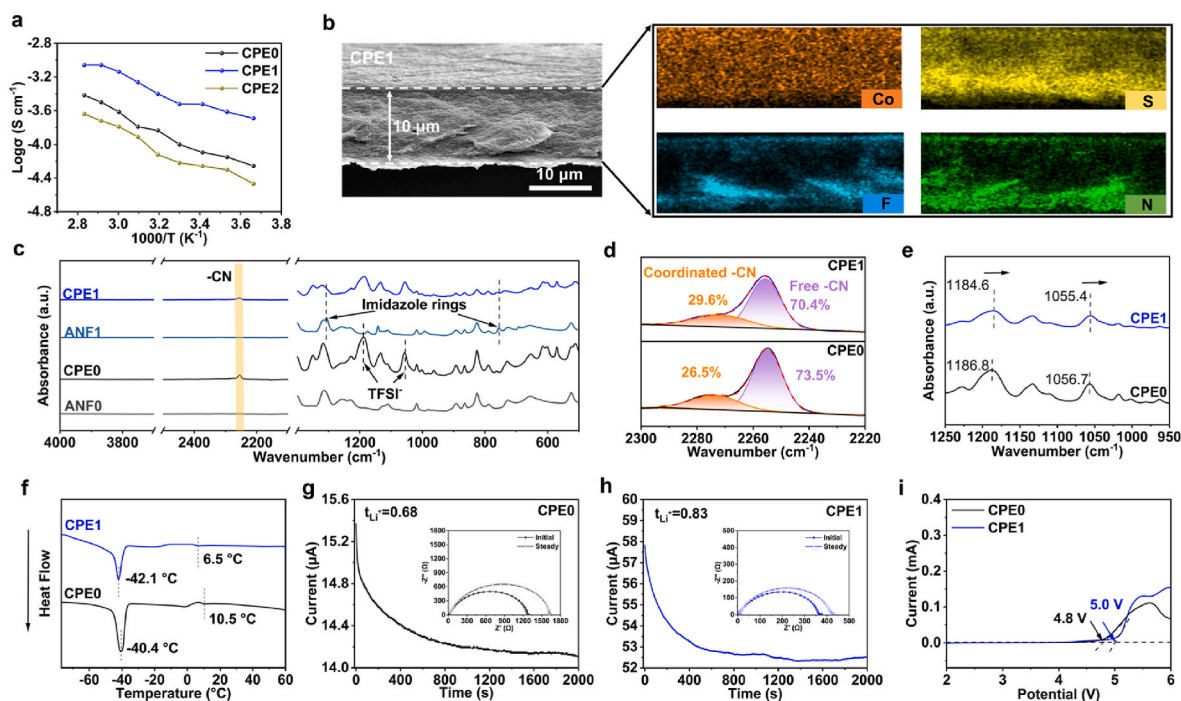


**Fig. 2.** (a) Ionic conductivity of the electrolytes. (b) Cross-sectional SEM image of the CPE1 membranes with the corresponding EDS element mappings of the Co, S, F and N elements. (c), (d) and (e) FTIR spectra of the ANF0, CPE0, ANF1 and CPE1 films. (f) DSC curves of the composite electrolytes. (g), (h) The chronoamperometry (CA) curve for the composite electrolyte at 30 °C (The inset was the EIS Nyquist chart before and after the polarization). (i) Linear sweep voltammetry (LSV) curves of the composite electrolytes.

$\text{cm}^{-2}$  mass loading (Guangdong Canrd New Energy Technology Co., Ltd.). 20  $\mu\text{L}$  FEC was added into the cathode to infiltrate the surface before the battery assembly, protecting interface of the cathodes. The charge/discharge voltage range was 2.5–3.8 V for LFP (1 C = 170 mAh  $\text{g}^{-1}$ ) and 2.8–4.25 V for NCM622 (1 C = 180 mAh  $\text{g}^{-1}$ ) cathodes at 30 °C.

### 3. Results and discussion

#### 3.1. Electrolyte design

The preparation process of the porous ANF network films is based on facile and scalable blade-casting and freeze-drying methods. First, the prepared ANF solution was deposited on glass slides via a blade-casting method. And the thickness of the coating layers was controllable by adjusting the gap of the scraper, which is conducive to reducing the electrolyte thickness and the preparation cost while maintaining the flexibility of the electrolytes [16]. After that, the ANF coating layers were immersed into deionized water to protonate the ANF for forming 3D continuous ANF networks [24–26]. And then, the 3D porous ANF network films were prepared after the drying process. Finally, the in situ grown ZIF-67 nanoparticles were formed on the pores of the networks by immersing into the 2-methylimidazole solution (Fig. S1). The thickness of the ANF skeleton films progressively increased with extended immersion time (i.e., ANF0, ANF1, ANF2 and ANF3 correspond to immersion times of 0, 1, 2 and 3 h, respectively) (Fig. 1a). Specifically, the thickness of ANF0, ANF1, ANF2 and ANF3 was 7, 8, 11 and 13  $\mu\text{m}$ , respectively. An appropriately designed pore size in the ANF skeleton films ensured optimal electrolyte matrix incorporation, consequently improving performance of electrolytes. Upon the formation of in situ ZIF-67 nanoparticles on the ANF networks, due to the immersing time increased, the number and the size of the ZIF-67 nanoparticles had undergone a significant change, which resulted that the pore size of the 3D ANF skeleton films initially increased and then decreased (Fig. 1b–e). After 3 h of immersion, a significant reduction in pore size was observed due to the considerable growth of particle dimensions and the severe

aggregation of particles (i.e., ANF3 skeleton films), which had an adverse effect on the preparation of electrolytes.

In order to further demonstrate the composition details of the resulted ANF skeleton films, Fourier transform infrared (FTIR) was carried out (Fig. 1f–h). The FTIR spectrum exhibited characteristic peaks at 1305.5 and 755.5  $\text{cm}^{-1}$ , corresponding to the stretching and bending vibrations of imidazole rings, respectively. Additionally, a distinct peak at 425.2  $\text{cm}^{-1}$  was attributed to the Co–N stretching vibration (Fig. S2). These findings confirm the successful in situ growth of ZIF-67 nanoparticles on the ANF network films (i.e., ANF1 and ANF2) [22]. Meanwhile, the typical -NH- characteristic peak and -C=O peak in the ANF exhibited apparent shifts. The -NH- peak shifted from 1541.6 to 1542.4  $\text{cm}^{-1}$ , and the -C=O peak shifted from 1647.5 to 1650.3  $\text{cm}^{-1}$ . These observed spectral shifts demonstrates the coordination between the ANF and the ZIF-67, ultimately leading to the formation of multifunctional ANF skeleton films.

#### 3.2. Effect of ZIF-67 on the composite electrolytes

The SN-LiTFSI electrolyte matrix was prepared by mixing SN and LiTFSI with a molar ratio of 20:1 to guarantee high ionic conductivity [16,27]. The molten SN–LiTFSI electrolyte was filled into the porous ANF skeleton films by a facile solution infusion method (Fig. S1 and Table S1), significantly reducing the complexity of the electrolyte preparation. After the drying process, the composite electrolytes were obtained (i.e., CPE0, CPE1 and CPE2). The ionic conductivities of various composite electrolytes were measured between 0 and 80 °C (Fig. 2a). The CPE1 membrane presented the highest ionic conductivity of 0.3  $\text{mS cm}^{-1}$  at 30 °C among all the composite electrolytes, three times higher than 0.1  $\text{mS cm}^{-1}$  for CPE0 (Table S2). Due to the larger particle size and partial aggregation of ZIF-67 nanoparticles within the ANF2 skeleton film, the ionic conductivity of the CPE2 is reduced compared to both the CPE0 and the CPE1 (Fig. 1). The cross-sectional SEM images of the CPE1 membrane were shown in Fig. 2b. The thickness of the membrane was approximately 10  $\mu\text{m}$ , which was conducive

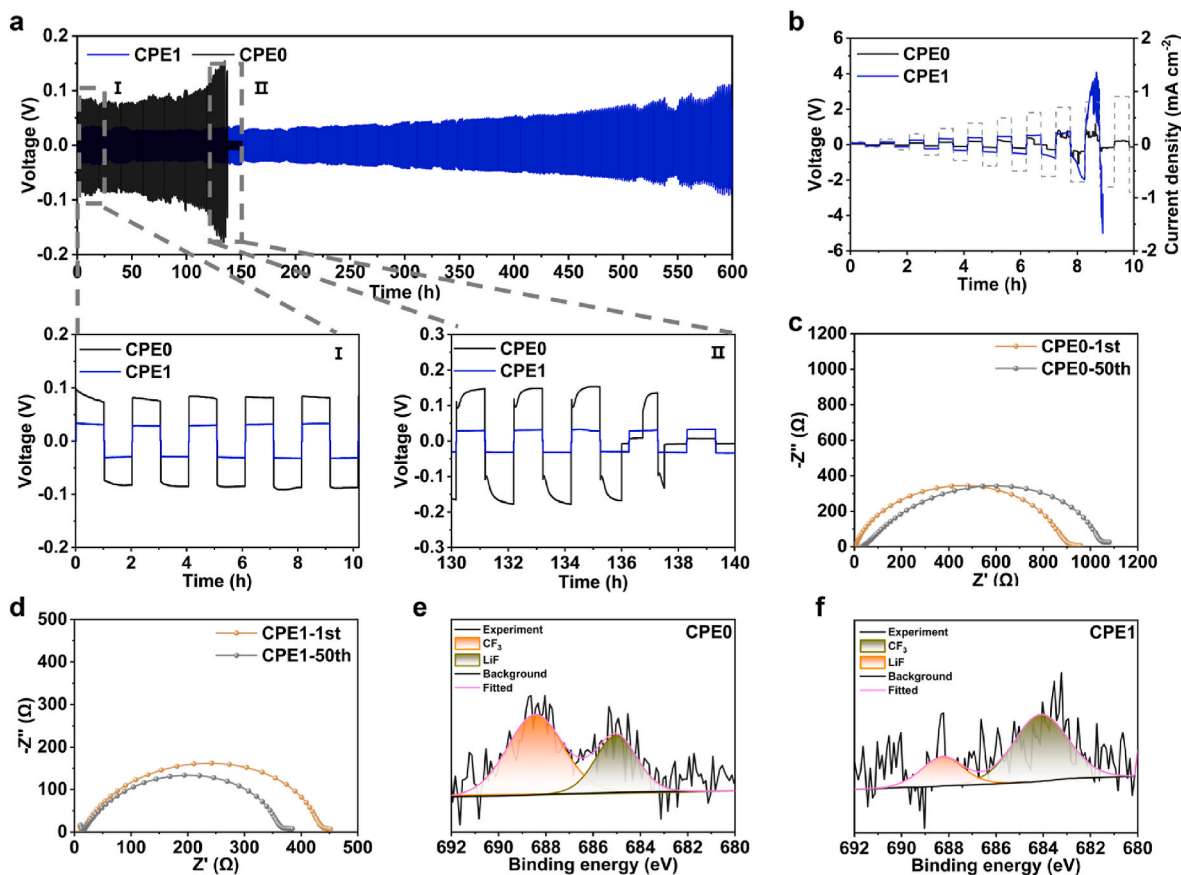


**Fig. 3.** (a) Long-term plating/stripping curves of the Li|CPE|Li cells at  $0.1 \text{ mA cm}^{-2}$ . The voltage-time profiles of symmetric Li||Li cells in the cycling interval of (I) 0–10 h, (II) 130–140 h. (b) Critical current density test of the Li||Li cells from  $0.05$  to  $0.9 \text{ mA cm}^{-2}$ . Nyquist plots of Li||Li cells with (c) the CPE0 electrolyte and (d) the CPE1 electrolyte after 50 cycles. XPS spectra of the cycled lithium anodes from the Li||Li symmetric batteries using (e) the CPE0 electrolyte and (f) the CPE1 electrolyte.

to lower ohmic resistance, greatly improving the electrochemical performance of batteries. The corresponding energy-dispersive spectral (EDS) mapping images of the CPE1 membrane verified that the SN-LiTFSI matrix was completely filled in the ANF1 skeleton films, and the ZIF-67 particles were uniformly distributed. The mechanical tensile stress-strain curves of the electrolyte films were shown in Fig. S3. The CPE0 membranes without the ZIF-67 particles exhibited the high ultimate tensile strength of  $19.8 \text{ MPa}$  with a low tensile strain of  $2.5 \%$ . In stark contrast, the CPE1 membranes with ZIF-67 particles showed an ultimate tensile strength of  $10.3 \text{ MPa}$  with a much higher tensile strain of  $7.8 \%$ . Due to the potential coordinate interaction between ZIF-67, LiTFSI and SN, the tensile strain of the CPE1 membranes significantly improved, which was three times than that of the CPE0 membranes. The CPE1 membranes can achieve a combination of high mechanical strength and good flexibility, which significantly inhibits lithium dendrite growth [3,28,29]. However, the CPE2 membranes exhibited significantly lower mechanical properties, with an ultimate tensile stress of just  $7.5 \text{ MPa}$  and strain of only  $6.7 \%$ , substantially inferior to those of CPE0 and CPE1 membranes. Considering that the significantly inferior mechanical properties and ionic conductivity of the CPE2 compared to CPE0 and CPE1 membranes, subsequent analyses were focused on CPE0 and CPE1 membranes.

The FTIR measurements of the composite electrolyte were shown in Fig. 2c. In CPE0 membranes, the peaks observed at  $1186.8$  and  $1057.6 \text{ cm}^{-1}$  in the CPE0 correspond to the S-N-S and C-F vibrational modes of LiTFSI. However, the S-N-S peak shifted from  $1186.8$  to  $1184.6 \text{ cm}^{-1}$  and the C-F peak shifted from  $1057.6$  to  $1055.4 \text{ cm}^{-1}$  in CPE1 membranes (Fig. 2e). Meanwhile, the characteristic peaks of the imidazole rings in the ZIF-67 particles at  $1305.5$  and  $755.5 \text{ cm}^{-1}$  disappeared.

These results demonstrated that the ZIF-67 served as Lewis acidic sites can complex with anions (TFSI<sup>-</sup>) in electrolyte matrix-filled pore channels, accelerating the dissociation and mobility of Li<sup>+</sup>, which was conducive to the improvement of the battery performance [23,30,31]. Generally, the -CN stretching vibration band can be separated into two bands. The peak at  $2254.8 \text{ cm}^{-1}$  corresponded to free -CN, and another peak at  $2273.3 \text{ cm}^{-1}$  presented the coordinated nitrile groups with metal atoms and groups [32]. In both CPE0 and CPE1 membranes, the two bands of -CN appeared (Fig. 2d). In the CPE1 system, the percentage of the coordinated nitrile groups was  $29.6 \%$ , which was higher than that of the CPE0 system ( $26.5 \%$ ). Because the ZIF-67 can absorb and immobilized TFSI<sup>-</sup> anions, enhancing Li<sup>+</sup> dissociation and releasing more Li<sup>+</sup>. The more Li<sup>+</sup> can complex with -CN groups of the SN molecules, which can effectively enhance ionic conductivity of the CPE1 and improve the battery performance.

Differential scanning calorimetry (DSC) measurements were also investigated the role of ZIF-67 in improving ionic conductivity of the CPE1 membranes. There were two endothermic peaks at  $-37.4$  and  $39.2 \text{ }^\circ\text{C}$  in the curves of the SN-LiTFSI electrolytes, corresponding to the transition temperature ( $T_{cp}$ ) from normal crystal to plastic crystal phase and the melting point ( $T_m$ ), respectively. Compared to the SN-LiTFSI electrolytes, the introduction of the ANF network led to lower  $T_m$  and  $T_{cp}$  of the CPE0 and CPE1. In the CPE1 system, the  $T_{cp}$  and  $T_m$  were found to occur at  $-42.1$  and  $6.5 \text{ }^\circ\text{C}$ , respectively, which were lower than those of the CPE0. These measurements demonstrated that ZIF-67 can decrease crystallinity and promote the formation of amorphous regions in the SN-LiTFSI, facilitating the gauche-to-trans isomerization of SN molecules while enhancing the Li<sup>+</sup> mobility, thereby increasing the ionic conductivity of the CPE1.

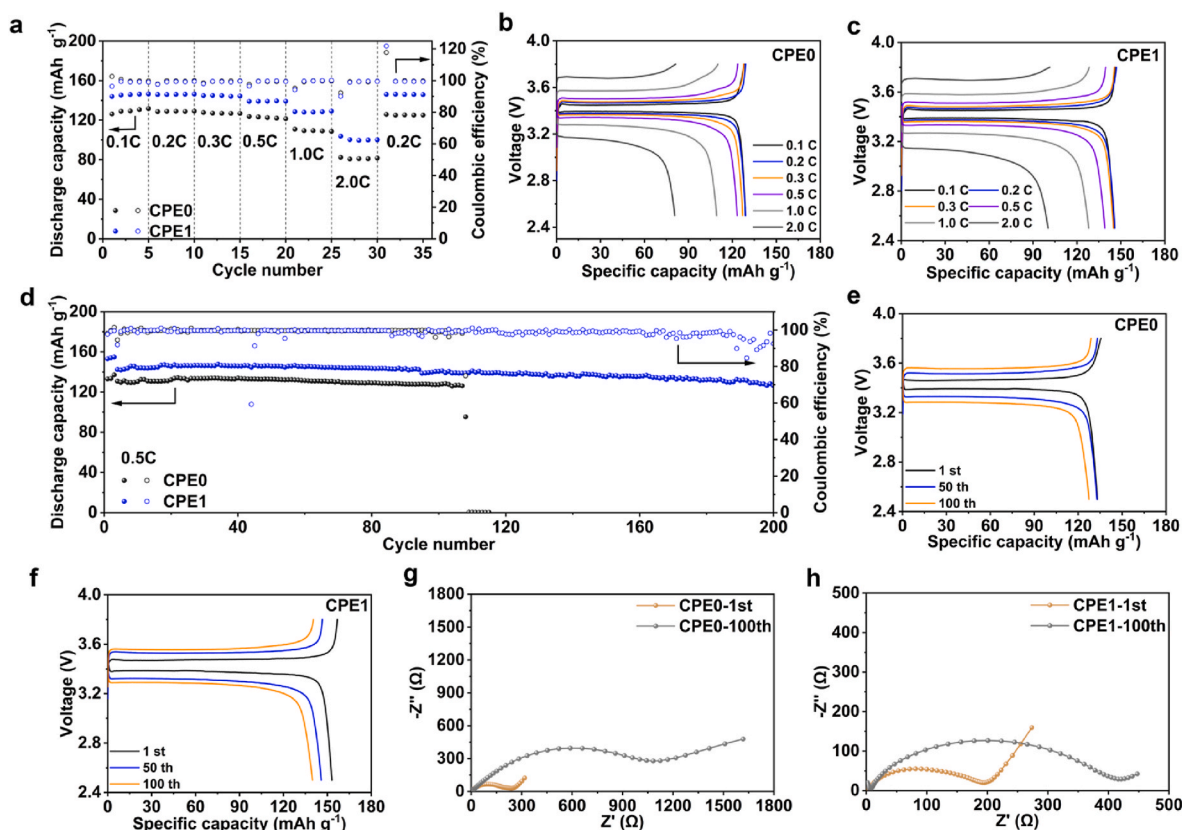


**Fig. 4.** (a) Rate performance of the solid-state Li||LFP cells at 30 °C. (b), (c) Typical charge-discharge profiles of the solid-state Li||LFP cells at various current densities. (d) Cycling performance of the solid-state Li||LFP cells at 30 °C. (e), (f) Typical charge-discharge profiles of the solid-state Li||LFP cells at different cycles. (g), (h) Nyquist plots of Li||LFP cells after 100 cycles.

The  $\text{Li}^+$  transference number ( $t_{\text{Li}^+}$ ) is also a crucial factor in evaluating the migration efficiency of  $\text{Li}^+$  in electrolytes, which is measured with the combination of chronoamperometry (CA) and electrochemical impedance spectroscopy (EIS). Because of the interaction between TFSI<sup>-</sup> anions and ZIF-67, the mobility of the anions was limited and the CPE1 membranes delivered a higher  $\text{Li}^+$  transference number of 0.83 than the CPE0 (0.68, Fig. 2g–h). Consistent with previous results, these results further confirmed that ZIF-67 served as Lewis acidic sites for TFSI<sup>-</sup> anions adsorption, which reduced anion mobility and improved the  $\text{Li}^+$  conduction. To evaluate the electrochemical stability of composite electrolytes, linear sweep voltammetry (LSV) measurements were employed to determine their electrochemical stability window. Compared to the CPE0 (4.8 V), the sweep range of the CPE1 was extended to 5.0 V without any obvious current peaks. Thus, the CPE1 membranes exhibited excellent compatibility with high-voltage cathode materials, making them promising candidates for high-performance LMBs.

### 3.3. Interfacial resistance against Li dendrites

The growth of lithium dendrites poses a significant threat to the cycling safety of lithium metal batteries. Owing to the presence of lithiophilic polar functional groups (e.g., amide groups), ANF can easily interact with  $\text{Li}^+$  and participate in the  $\text{Li}^+$  transport. Meanwhile, the in situ grown ZIF-67 nanoparticles selectively complex with TFSI<sup>-</sup> anions, which promotes  $\text{Li}^+$ -TFSI<sup>-</sup> dissociation and enhances the  $\text{Li}^+$  ion mobility. As a result, the CPE1 shows high ionic conductivity, exceptional  $\text{Li}^+$  transference number. Furthermore, the electrolyte also possesses sufficient mechanical strength. Thus, the CPE1 is expected to provide excellent dynamic electrochemical stability and interfacial stability toward lithium metal. Li symmetrical cells with composite

electrolytes were assembled to investigate interfacial stability between electrolytes and lithium metal. As shown in Fig. 3a, the Li|CPE1|Li cell stably cycled for over 600 h with a low initial overpotential of 35 mV at 0.1 mA cm<sup>-2</sup> and 30 °C. Moreover, the smooth voltage profiles of the Li|CPE1|Li cells at different stages (0–10, 130–140 h) demonstrated that the CPE1 showed excellent electrochemical stability towards lithium metal. However, the Li|Li cell with CPE0 delivered a higher initial overpotential of 96 mV. And the cell suffered a rapid voltage increase during the cycling process. After 137 h of cycling, a sharp and irreversible voltage drop in CPE0-based Li|Li cell was observed, indicating that a dendrite-induced short circuit in the cell. Meanwhile, the critical current density of the Li|Li cells was also tested to access their electrochemical stability under high-current conduction (Fig. 3b). Notably, the Li|CPE1|Li cell exhibited a higher critical current density of 0.8 mA cm<sup>-2</sup> compared to that of the Li|CPE0|Li (0.6 mA cm<sup>-2</sup>). The improved interfacial stability between SN-based electrolytes and lithium metal in Li|CPE1|Li cell is attributed to the high ionic conductivity,  $\text{Li}^+$  transference number and mechanical strength of the CPE1.

In addition, electrochemical impedance spectroscopy (EIS) was employed to quantitatively access the interfacial compatibility between the electrolytes and lithium metal (Fig. 3c–d). EIS measurement was conducted on Li|Li cells with the CPE0 and CPE1 at the initial cycle and 50 cycles. At the initial cycle, the interfacial resistance of the Li|CPE0|Li cell was 900 Ω, which was much higher than that of the Li|CPE1|Li cell (370 Ω). After 50 cycles, a much small impedance change can be observed in the Li|CPE1|Li cell, the values of impedance increased from 370 to 435 Ω, suggesting a more stable interface inside the cell. In stark contrast, the impedance of the Li|CPE0|Li cell increased significantly, indicating that the severe side reactions between SN and lithium metal at the interface, resulting in uncontrolled solid electrolyte interface (SEI) growth and compromising interfacial kinetics (Fig. S4).



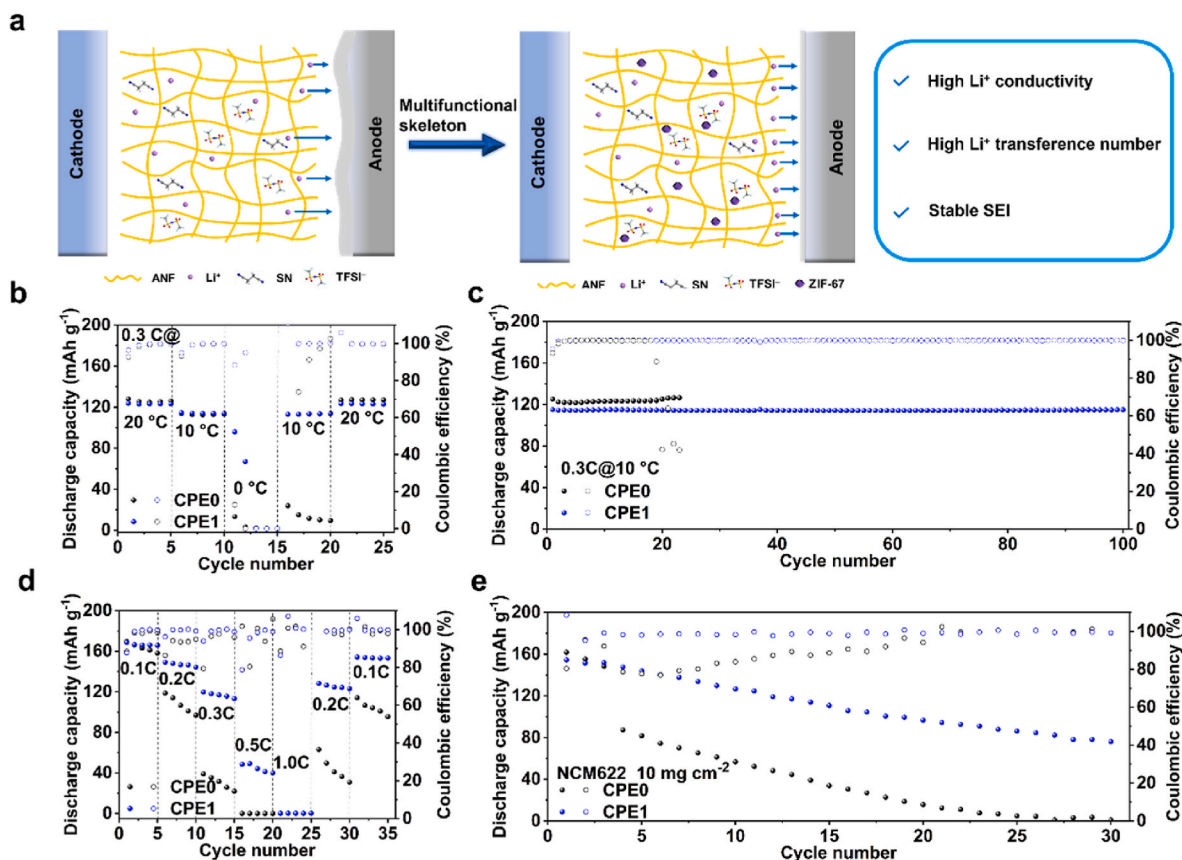


Fig. 5. (a) Schematic illustration of the effect of the multifunctional skeletons on LMBs. (b) Rate performance of the solid-state Li||LFP cells at 0.3 C and low temperatures. (c) Cycling performance of the solid-state Li||LFP cells at 0.3 C and 10 °C. (d) Rate performance of the solid-state Li||NCM622 cells at 30 °C. (e) Cycling performance of the solid-state Li||NCM622 cells at 0.1 C and 30 °C.

To unveil the reason for the improved interfacial stability between CPE1 and lithium metal, the chemical composition of the SEI layer was further investigated by X-ray photoelectron spectroscopy (XPS). There were two prominent peaks at 684.8 and 688.2 eV, corresponding to CF<sub>3</sub> and LiF peak, respectively, which originated from the decomposition of LiTFSI (Fig. 3e–f). Compared to the CPE0, the lithium metal surface in contact with the CPE1 showed a significantly higher LiF content after extensive plating-stripping, indicating that LiTFSI underwent more pronounced decomposition in the Li|CPE1|Li cell [17]. The LiF-rich SEI acted as an effective electronic insulator, inhibiting the parasitic reaction between Li metal and the electrolyte while facilitating uniform decomposition. Thus, the CPE1 is beneficial for smooth Li plating and stripping and inhibiting lithium dendrite growth.

### 3.4. Solid-state metallic lithium battery performance

The composite electrolytes demonstrated favorable ion transport kinetics and interfacial characteristic, suggesting strong potential for practical application in solid-state battery systems. To evaluate the potential utility of composite electrolyte at ambient temperature, all-solid-state lithium metal batteries were assembled with LiFePO<sub>4</sub> (LFP) and high-voltage LiNi<sub>0.6</sub>Co<sub>0.2</sub>Mn<sub>0.2</sub>O<sub>2</sub> (NCM622) cathodes. As shown in Fig. 4a, the Li|CPE1|LFP cell presented discharge capacities of 146.2, 146.1, 144.9, 139.2, 128.1 and 99.6 mAh g<sup>-1</sup> at 0.1, 0.2, 0.3, 0.5, 1.0 and 2.0 C, respectively. When the current density was restored to 0.2 C, the discharge capacity of the cell returned to 145.9 mAh g<sup>-1</sup>, demonstrating the excellent reversibility and rate performance of the Li|CPE1|LFP cell. For the Li|CPE0|LFP cell, the discharge capacity was much lower than that of the Li|CPE1|LFP at different rates range from 0.1 to 2.0 C. Notably, the cell only exhibited discharge capacity of 81.1 mAh

g<sup>-1</sup> at high rate of 2.0 C. Additionally, the Li|CPE1|LFP cell showed lower overpotentials as the current density increased (Fig. 4b–c).

The long-term cycling performance of the Li||LFP cells was shown in Fig. 4d. The Li|CPE1|LFP cell delivered an initial discharge capacity of 145.8 mAh g<sup>-1</sup> after the first activation process. And the cell showed exceptional stability with minimal capacity degradation at 0.5 C over 200 cycles with a capacity retention of 90%. In comparison, following the first activation process, the Li|CPE0|LFP cell showed an initial discharge capacity of 137.1 mAh g<sup>-1</sup>, and the cell suffered from rapid capacity decay to 0 mAh g<sup>-1</sup> within 110 cycles. In addition, with prolong cycling, the CPE1-based cells showed a small overpotential, especially after 50 cycles (Fig. 4e–f). And the Li|CPE1|LFP cell also displayed few changes of interfacial resistance during cycling process than that of the Li|CPE0|LFP cell (Fig. 4g–h). The excellent cycling stability can be attributed to high Li<sup>+</sup> transference number due to the selective absorption of the ZIF-67, facilitating the mobility of Li<sup>+</sup> and uniform Li deposition. On the other hand, the LiF-rich SEI layer between electrolytes and lithium metal also reduced the emergence of side reactions between SN and lithium metal, ensuring the long cycle stability of the solid-state LMBs (Fig. 5a).

To access the practical applicability of the battery system, the electrochemical performance of Li||LFP cells under low-temperature operating conditions was investigated. As shown in Fig. 5b, the Li|CPE1|LFP cell delivered discharge capacities of 123.8 and 114.5 mAh g<sup>-1</sup> at 20 and 10 °C, respectively. Upon cycling at 0 °C and subsequent temperature increase, the discharge capacity recovered to 113.7 and 123.3 mAh g<sup>-1</sup> at 10 and 20 °C, demonstrating excellent capacity retention and temperature adaptability of the Li|CPE1|LFP cell. In contrast, the Li|CPE0|LFP cell showed poorer performance, exhibiting only 10 mAh g<sup>-1</sup> when the temperature returned to 10 °C. Although the CPE0-based cell

initially delivered a high discharge capacity of 125.3 mAh g<sup>-1</sup> at 10 °C, it showed poor cycling stability with Coulombic efficiency rapidly decaying to 50 % within just 20 cycles (Fig. 5c). However, the Li|CPE1|LFP cell displayed a steady cycling process for more than 100 cycles with a high-capacity retention of 99 %. The practical feasibility of composite electrolytes was systematically examined using Li||NCM622 cells with high mass loading of 10 mg cm<sup>-2</sup>. The Li|CPE0|NCM622 cell showed rapid capacity decay at 0.2 C, resulting from the slow Li<sup>+</sup> mobility and the serious side reaction between the electrolyte and lithium metal anodes (Fig. 5d). In addition, the Li|CPE1|NCM622 cell exhibited superior long-term cycling performance, indicating excellent viability for high-voltage battery system (Fig. 5e). These results clearly illustrate the SN-based electrolytes with multifunctional skeletons showed great potentials for applicability in solid-state LMBs.

#### 4. Conclusion

An ultrathin solid-state electrolyte membrane is constructed by filling SN-LiTFSI electrolyte into an ultrathin multifunctional functional skeleton via facile solution infusion method. The designed composite electrolyte shows a 10 μm-ultrathin thickness, remarkable mechanical strength with a tensile strength of 10 MPa. Importantly, it also exhibits superior electrochemical properties, including a high ionic conductivity of 3 × 10<sup>-4</sup> S cm<sup>-1</sup> and Li<sup>+</sup> transference number of 0.83 at room temperature. The detail analysis indicates that the in situ grown ZIF-67 nanoparticles can selectively absorb TFSI<sup>-</sup> anions and facilitate the formation of LiF-rich SEI layer to mitigate the side reaction between SN and lithium metal. In virtue of these advantages, the composite electrolyte-based Li||LFP cell delivers superior long-cycling performance and rare capability at room temperature and 10 °C. This work develops a scalable fabrication method for ultrathin solid-state electrolyte with ultrahigh Li<sup>+</sup> transference number, addressing critical challenges for the practical application of solid-state lithium metal batteries.

#### CRedit authorship contribution statement

**Dongmei Zhang:** Writing – original draft, Methodology, Data curation, Conceptualization. **Dingrong Long:** Writing – review & editing, Visualization, Validation. **Jiangping Zhang:** Investigation, Formal analysis, Data curation. **Jiaxin Tu:** Writing – review & editing, Visualization, Resources. **Baoyi wang:** Writing – review & editing, Visualization, Methodology. **Rubing Xu:** Writing – review & editing, Validation, Data curation. **Kunda Yang:** Writing – review & editing, Methodology, Investigation. **Qianxiao Fan:** Supervision, Resources, Project administration, Conceptualization. **Wendi Zhang:** Writing – review & editing, Project administration, Methodology. **Lehao Liu:** Writing – review & editing, Supervision, Resources, Funding acquisition. **Meicheng Li:** Writing – review & editing, Validation, Supervision, Funding acquisition.

#### Declaration of competing interest

The authors declare that they have no known competing financial interests or personal relationships that could have appeared to influence the work reported in this paper.

#### Acknowledgements

This work is supported partially by project of National Natural Science Foundation of China (52272200, 52302250), Hebei Natural Science Foundation (E2022502022), the project of China Three Gorges Corporation named key technologies of intelligent joint regulation and operation with grid connected friendly in power station group of wind, solar photovoltaic and energy storage (WWKY-2021-0173), Huaneng Group Headquarters Science and Technology Project (HNKJ20-H88), and the NCEPU "Double First-Class" Program.

#### Appendix A. Supplementary data

Supplementary data to this article can be found online at <https://doi.org/10.1016/j.jpowsour.2025.238312>.

#### Data availability

Data will be made available on request.

#### References

- [1] J. Wan, J. Xie, X. Kong, Z. Liu, K. Liu, F. Shi, A. Pei, H. Chen, W. Chen, J. Chen, X. K. Zhang, L.Q. Zong, J.Y. Wang, L.Q. Chen, J. Qin, Y. Cui, Ultrathin, flexible, solid polymer composite electrolyte enabled with aligned nanoporous host for lithium batteries, *Nat. Nanotechnol.* 14 (2019) 705–711.
- [2] M.H. Zhou, R.L. Liu, D.Y. Jia, Y. Cui, Q.T. Liu, S.H. Liu, D.C. Wu, Ultrathin yet robust single lithium-ion conducting quasi-solid-state polymer-brush electrolytes enable ultralong-life and dendrite-free lithium-metal batteries, *Adv. Mater.* 33 (2021) 2100943.
- [3] F. He, W. Tang, X. Zhang, L. Deng, J. Luo, High energy density solid state lithium metal batteries enabled by Sub-5 μm solid polymer electrolytes, *Adv. Mater.* 33 (2021) 2105329.
- [4] J.M. Whiteley, P. Taynton, W. Zhang, S.H. Lee, Ultrathin Solid-state Li-ion electrolyte membrane facilitated by a self-healing polymer matrix, *Adv. Mater.* 27 (2015) 6922–6927.
- [5] L. Yang, D. Luo, Y. Zheng, T. Yang, Q. Ma, Y. Nie, H. Dou, Y. Zhang, R. Huang, A. Yu, L. Shui, X. Wang, Z. Chen, Heterogeneous nanodomain electrolytes for ultra-long-life all-solid-state lithium-metal batteries, *Adv. Funct. Mater.* 32 (2022) 2204778.
- [6] D. Huang, M. Kamiko, S. Yagi, Synthesis conditions affecting electrochemical and chemical stabilities of Ga-doped Li<sub>7</sub>La<sub>3</sub>Zr<sub>2</sub>O<sub>12</sub> solid electrolyte, *EcoEnergy* 2 (2024) 141–153.
- [7] Y. Liu, F. Fu, H. Teng, Y. Sun, S. Zhang, A. Zhang, N. Zhang, R. Jing, L. Cong, H. Xie, L. Sun, Dual-phase elastomeric electrolyte with a latitude-longitude interwoven structure for high-energy solid-state lithium metal batteries, *Adv. Energy Mater.* 14 (2024) 2402040.
- [8] L. Tang, B. Chen, Z. Zhang, C. Ma, J. Chen, Y. Huang, F. Zhang, Q. Dong, G. Xue, D. Chen, C. Hu, S. Li, Z. Liu, Y. Shen, Q. Chen, L. Chen, Polyfluorinated crosslinker-based solid polymer electrolytes for long-cycling 4.5 V lithium metal batteries, *Nat. Commun.* 14 (2023) 2301.
- [9] D. Zhang, Z. Luo, H. Xu, Y. Guo, H. Chen, Y. Ye, J. An, J. Hui, Y. Shi, S. Yang, B. Li, Liberating lithium ions from polymer matrix via harnessing ion-dipole interaction toward stable solid-state lithium metal batteries, *Adv. Funct. Mater.* 34 (2024) 2409134.
- [10] Z. Liu, S. Peng, P. Xiaokaiti, J. Zhang, H. You, A. Abudula, G. Guan, Electrothermal model of all-solid-state lithium battery with composite solid-state electrolyte, *EcoEnergy* 1 (2023) 414–424.
- [11] H. Xu, J. Yang, Y. Niu, X. Hou, Z. Sun, C. Jiang, Y. Xiao, C. He, S. Yang, B. Li, W. Chen, Deciphering and integrating functionalized side chains for high ion-conductive elastic ternary copolymer solid-state electrolytes for safe lithium metal batteries, *Angew. Chem., Int. Ed.* 63 (2024) e202406637.
- [12] M. Li, T. Tian, X. Yang, Y. He, D. Zhang, P. Müller-Buschbaum, S. Yang, B. Li, Analogue molecular doping engineering enables high ionic conductivity of polyvinylidene fluoride-based polymer electrolytes, *ACS Nano* 19 (2025) 20084–20095.
- [13] T.L. Jiang, P.G. He, G.X. Wang, Y. Shen, C.W. Nan, L.Z. Fan, Solvent-free synthesis of thin, flexible, nonflammable garnet-based composite solid electrolyte for all-solid-state lithium batteries, *Adv. Energy Mater.* 10 (2020) 1903376.
- [14] K.H. Choi, S.J. Cho, S.H. Kim, Y.H. Kwon, J.Y. Kim, S.Y. Lee, Thin, deformable, and safety-reinforced plastic crystal polymer electrolytes for high-performance flexible lithium-ion batteries, *Adv. Funct. Mater.* 24 (2014) 44–52.
- [15] J. Sun, C. He, X. Yao, A. Song, Y. Li, Q. Zhang, C. Hou, Q. Shi, H. Wang, Hierarchical composite-solid-electrolyte with high electrochemical stability and interfacial regulation for boosting ultra-stable lithium batteries, *Adv. Funct. Mater.* 31 (2021) 2006381.
- [16] D. Zhang, X. Meng, W. Zhang, J. Mo, Q. Zhao, B. Wang, Q. Fan, L. Liu, T. Yang, Y. Jin, R. Zhou, M. Zhang, M. Li, A thin and ultrahigh-ionic-conductivity composite electrolyte with 3D aramid nanofiber networks toward ambient-temperature lithium metal batteries, *Adv. Energy Mater.* 15 (2024) 2403565.
- [17] X. Ye, H. Fu, Y. Zhang, D. Wu, Y. Zhong, X. Wang, X. Ouyang, J. Tu, Modulating the Li-Ion transport pathway of succinonitrile-based plastic crystalline electrolytes for solid-state lithium metal batteries, *Adv. Funct. Mater.* 35 (2025) 2413205.
- [18] H. Wu, B. Tang, X.F. Du, J.J. Zhang, X.R. Yu, Y.T. Wang, J. Ma, Q. Zhou, J.W. Zhao, S.M. Dong, G.J. Xu, J.N. Zhang, H. Xu, G.L. Cui, L.Q. Chen, LiDFOB initiated in situ polymerization of novel eutectic solution enables room-temperature solid lithium metal batteries, *Adv. Sci.* 7 (2020) 2003370.
- [19] A. Wang, S. Geng, Z. Zhao, Z. Hu, J. Luo, In situ cross-linked plastic crystal electrolytes for wide-temperature and high-energy-density lithium metal batteries, *Adv. Funct. Mater.* 32 (2022) 2201861.
- [20] C. Li, H. Yue, Q. Wang, J. Li, J. Zhang, H. Dong, Y. Yin, S. Yang, A novel composite solid polymer electrolyte based on copolymer P(LA-co-TMC) for all-solid-state lithium ionic batteries, *Solid State Ionics* 321 (2018) 8–14.



- [21] R. Dong, J. Zheng, J. Yuan, Y. Li, T. Zhang, Y. Liu, Y. Liu, Y. Sun, B. Zhong, Y. Chen, Z. Wu, X. Guo, A polyethylene oxide/metal-organic framework composite solid electrolyte with uniform Li deposition and stability for lithium anode by immobilizing anions, *J. Colloid Interface Sci.* 620 (2022) 47–56.
- [22] X. Song, K. Ma, J. Wang, H. Wang, H. Xie, Z. Zheng, J. Zhang, Three-dimensional metal-organic framework@cellulose skeleton-reinforced composite polymer electrolyte for all-solid-state lithium metal battery, *ACS Nano* 18 (2024) 12311–12324.
- [23] X. Wang, C. Zhao, B. Liu, S. Zhao, Y. Zhang, L. Qian, Z. Chen, J. Wang, X. Wang, Z. Chen, Creating edge sites within the 2D metal-organic framework boosts redox kinetics in lithium-sulfur batteries, *Adv. Energy Mater.* 12 (2022) 2201960.
- [24] P.Y. Hu, J. Lyu, C. Fu, W.B. Gong, J.H. Liao, W.B. Lu, Y.P. Chen, X.T. Zhang, Multifunctional aramid nanofiber/carbon nanotube hybrid aerogel films, *ACS Nano* 14 (2020) 688–697.
- [25] B. Yang, L. Wang, M.Y. Zhang, J.J. Luo, Z.Q. Lu, X.Y. Ding, Fabrication, applications, and prospects of aramid nanofiber, *Adv. Funct. Mater.* 30 (2020) 2000186.
- [26] C.J. Xie, Z.X. Guo, T. Qiu, X.L. Tuo, Construction of aramid engineering materials via polymerization-induced para-Aramid nanofiber hydrogel, *Adv. Mater.* 33 (2021) 2101280.
- [27] P.-J. Alarco, Y. Abu-Lebdeh, A. Abouimrane, M. Armand, The plastic-crystalline phase of succinonitrile as a universal matrix for solid-state ionic conductors, *Nat. Mater.* 3 (2004) 476–481.
- [28] Z. Wang, L. Shen, S. Deng, P. Cui, X. Yao, 10  $\mu\text{m}$ -thick high-strength solid polymer electrolytes with excellent interface compatibility for flexible all-solid-state lithium-metal batteries, *Adv. Mater.* 33 (2021) 2100353.
- [29] L. Gao, S.B. Luo, J.X. Li, B.W. Cheng, W.M. Kang, N.P. Deng, Core-shell structure nanofibers-ceramic nanowires based composite electrolytes with high Li transference number for high-performance all-solid-state lithium metal batteries, *Energy Storage Mater.* 43 (2021) 266–274.
- [30] Q. Yang, R. Lu, S. Ren, C. Chen, Z. Chen, X. Yang, Three dimensional reduced graphene oxide/ZIF-67 aerogel: effective removal cationic and anionic dyes from water, *Chem. Eng. J.* 348 (2018) 202–211.
- [31] Y. Zheng, N. Yang, R. Gao, Z. Li, H. Dou, G. Li, L. Qian, Y. Deng, J. Liang, L. Yang, Y. Liu, Q. Ma, D. Luo, N. Zhu, K. Li, X. Wang, Z. Chen, “Tree Trunk” design for flexible quasi solid-state electrolyte with hierarchical ion-channels enabling ultralong-life lithium metal batteries, *Adv. Mater.* 34 (2022) 2203417.
- [32] Y.-N. Yang, F.-L. Jiang, Y.-Q. Li, Z.-X. Wang, T. Zhang, A surface coordination interphase stabilizes a solid-state battery, *Angew. Chem., Int. Ed.* 60 (2021) 24162–24170.